

Sonoprinting in 3D: liposome-loaded microbubbles and ultrasound promote drug delivery in tumor spheroids

S. Roovers^{1,2}, J. Deprez^{1,2}, D. Priwitaningrum³, G. Lajoinie⁴, N. Rivron⁵, H. De Clercq^{2,6}, O. De Wever^{2,7}, E. Stride⁸, S. Le Gac⁹, M. Versluis⁴, J. Prakash³, S.C. De Smedt^{1,2*}, I. Lentacker^{1,2*}

¹Laboratory of General Biochemistry and Physical Pharmacy, Ghent Research Group on Nanomedicine, Ghent University, Ghent, Belgium

²Cancer Research Institute Ghent (CRIG), Ghent, Belgium

³Targeted Therapeutics, Department of Biomaterials Science and Technology, MIRA Institute, University of Twente, Enschede, The Netherlands

⁴Physics of Fluids Group, MESA+ Institute for Nanotechnology and Technical Medical (TechMed) Center, University of Twente, Enschede, The Netherlands

⁵Department of Complex Tissue Regeneration, MERLN Institute for Technology-Inspired Regenerative Medicine, Maastricht University, Maastricht, The Netherlands

⁶Department of Basic Medical Sciences, Ghent University, Ghent, Belgium

⁷Laboratory Experimental Cancer Research (LECR), Ghent University, Ghent, Belgium

⁸Institute of Biomedical Engineering, Department of Engineering Science, University of Oxford, Oxford, UK

⁹Applied Microfluidics for BioEngineering Research, MIRA Institute, University of Twente, Enschede, The Netherlands

- Equal contribution of last authors

Abstract

Ultrasound-triggered drug-loaded microbubbles have shown great potential for drug delivery purposes due to their ability to locally release drugs and simultaneously enhance their delivery into the target tissue. Recently, we have proposed “sonoprinting” as an alternative mechanism that may be responsible for the ultrasound-triggered delivery of nanoparticles from nanoparticle-loaded microbubbles. Sonoprinting leads to the local deposition of nanoparticles and microbubble shell fragments in 2D cell cultures. However, the confined space and reflective membrane present in a 2D cell culture, can cause asymmetrical oscillations of microbubbles and as such influence microbubble-cell interactions. This work therefore focused on the further exploration of the sonoprinting phenomenon on free-floating 3D multicellular spheroids to verify whether sonoprinting can also occur in more complex biological tissues. Our results show that sonoprinting can be a very powerful tool to deliver high amounts of nanoparticles to the outer layers of 3D tumor spheroids, followed by a complete drug release into the deeper layers of the tumor spheroid. Sonoprinting significantly enhanced the cytotoxicity of both Doxil[®]-like and ThermoDOX[®]-like liposomes. We also give proof that only the microbubble associated nanoparticles become printed, indicating that substantially lower drug doses are effective. In conclusion, we show that sonoprinting can also occur in a more complex multicellular environment and is a very interesting tool to achieve ultrasound-triggered drug delivery by locally depositing nanoparticles as drug reservoirs in close proximity to target sites.

Introduction

Despite the many effective anti-cancer agents available, successful clinical treatment of tumors remains challenging. One of the major reasons is that the dose of these anti-cancer agents is typically limited, as they can induce severe toxicity due to their non-selective nature. An attractive solution is to encapsulate these small molecules into nanoparticles. Nanomedicines are believed to solely penetrate tumorous tissue based on the enhanced permeation and retention (EPR) effect^{1,2}. This effect originates from enlarged openings in the endothelial barriers and inefficient removal of products due to underdeveloped blood and lymph vessels, which are believed to arise in fast growing tumors. Although nanoparticles have been extensively studied with numerous successes in preclinical models, clinical studies have only shown limited therapeutic benefits^{3,4}. This mismatch in effectiveness can be explained by the overestimation of the EPR effect in a clinical context^{2,5,6}. Although the EPR effect is often present in animal models, a large heterogeneity is seen amongst and within human tumors^{2,6}. Nanoparticles remain however very attractive due to their tunable nature; their ability to increase the solubility and plasma half-life of (poorly soluble) drugs; the ability to protect bioactive substances, such as proteins or genetic drugs, from premature degradation and to promote the cellular uptake of drugs via endosomal pathways. In order to increase intratumoral uptake of nanomedicines, other delivery strategies that rely on active targeting approaches are currently under investigation. Among these strategies, physical triggers are of particular interest since they do not require the presence of specific ligands and their efficacy is not affected by changes in the expression of their target. Possible physical stimuli that could induce local drug delivery include magnetism, thermal activity, light and ultrasound^{2,7,8}.

In our group, we focus on ultrasound-triggered drug delivery since it is a well-known, cheap and relatively safe method that has advantages for both imaging and therapy. Ultrasound can be combined with lipid-shelled micron-sized gas bubbles, called microbubbles, which respond to ultrasound by cavitating, i.e. expanding and contracting along with the pressure phases of the ultrasound wave. The strong echo arising from cavitation explains the use of microbubbles as contrast agents for ultrasound imaging. Additionally, microbubbles are also used as drug carriers, since ultrasound-induced cavitation can facilitate spatial and temporal control of drug release and has been shown to promote the uptake of drugs and nanoparticles in tumors⁹. For long, the two main mechanisms that were commonly believed to be responsible for this improved delivery are sonoporation, i.e. the formation of small pores in cell membranes or the opening of tight junctions, and enhanced endocytosis⁹⁻¹¹. In the past, we and other groups have shown that microbubble loading can significantly increase the cellular uptake of nanoparticles compared to coadministering nanoparticles with microbubbles, indicating that a third mechanism might be at play here. Earlier, we proposed 'sonoprinting' as a mechanism that can

explain this observation¹². During sonoprinting, nanoparticles become released from cavitating nanoparticle-loaded microbubbles and are deposited onto target cells along with parts of the microbubble shell. Only recently, we elucidated the biophysical microbubble-cell interactions that are responsible for sonoprinting and which acoustic settings are optimal to induce it¹³. Since this study was performed in a static *in vitro* setup using adherent cells, it was not completely clear which impact the presence of a solid boundary has on the observed microbubble behavior. Indeed, it has been shown that the presence of such a boundary can cause asymmetrical oscillations of microbubbles and as such influence biophysical interactions with the cells^{14–16}. Furthermore, since the nanoparticle delivery was only evaluated on a single cell layer, questions on the significance of this mechanism in a tumor mass containing multiple cell layers remained. To assure that this sonoprinting phenomenon is not an artefact caused by the interactions of the microbubbles with the nearby membrane and to investigate the interactions of nanoparticle-loaded microbubbles with avascular tumor nodules containing multiple cell layers, this study focuses on drug delivery in multicellular 3D spheroid cultures.

Multicellular spheroids mimic the *in vivo* situation more closely due to their enhanced cell-to-cell contact, while maintaining the controlled environment of an *in vitro* study. Additionally, they can be made even more *in vivo*-like by including multiple cell types that make up the tumor microenvironment, such as tumor-associated fibroblasts and immune cells^{17–21}. The 3D microenvironment in these cultures strongly resembles the *in vivo* situation, as an extracellular matrix is formed that acts as a major physical barrier for drug penetration²². Spheroids consisting of various cell types have been extensively used in research and have revealed that several treatments are less effective in these models, compared to classical 2D monolayer systems^{22–25}. Even though these models lack an intact vasculature, they are a powerful research tool as they resemble the cellular complexity of the *in vivo* situation while providing mechanistic insight under well-controlled acoustic settings.

In this study, we evaluated the doxorubicin delivery in tumor spheroids when using ultrasound-triggered microbubbles carrying doxorubicin-loaded liposomes (DOX-liposomes). Specifically, we aimed to investigate the role of sonoprinting in the microbubble-assisted nanoparticle delivery to a soft tissue environment. Therefore, we first studied the delivery and localization of inert fluorescent polystyrene beads and ‘empty’ fluorescently labeled liposomes to tumor spheroids using flow cytometry and confocal imaging. Secondly, we loaded the liposomes with doxorubicin and used flow cytometry and confocal imaging of intact spheroids and cryosections to estimate drug release and distribution within monospheroids (4T1) and cospheroids (4T1 and NIH/3T3). Both regular and thermosensitive liposomes were used to evaluate the release of DOX from the printed liposomes and their distribution within the tumor spheroid. Additionally various toxicity assays were used to verify whether sonoprinting could enhance the efficacy of DOX-liposomes. Finally, we optimized the

microbubble formulation to minimize the presence of free liposomes in the sample, and confirmed that the efficiency of sonoprinting is caused by microbubble-loaded liposomes.

Materials and methods

Cell culture

4T1 murine breast cancer cells (ATCC, Manassas, VA, USA), 4T1 Luciferase positive cells (courtesy of the lab of Prof. Olivier De Wever) and NIH/3T3 fibroblast cells (ATCC) were grown in culture flasks in a humidified atmosphere with 5% CO₂ at 37°C. The culture medium for the 4T1 cells was RPMI (Gibco™, Thermo Fisher Scientific, Waltham, WA, USA), supplemented with 10% (v/v) fetal bovine serum (Hyclone, Thermo Fisher Scientific, MA, USA), 20 U/mL penicillin-streptomycin (Gibco™) and 2 mM L-glutamine (Gibco™). For the NIH/3T3 cells, Dulbecco's Modified Eagle Medium (Gibco™), supplemented with the same products was used.

Spheroid culturing and characterization

Multicellular spheroids were made by harvesting NIH/3T3 and 4T1 cells using 0.25% (w/v) Trypsin - EDTA solution (Gibco™) and transferring them to a custom-made agarose-based microwell array, developed by the Rivron Lab (MERLN institute, Maastricht, The Netherlands)²⁶. Approximately 500 cells were seeded per spheroid and one microwell array chip was able to form 1500 spheroids, which were cultured for 48h to form spheroids. The microwells were either filled with 4T1 cells only (monospheroids) or NIH/3T3 and 4T1 cells in a 5:1 ratio (co-spheroids), in accordance with previous work²⁷. After 48h, medium was removed and the spheroids were flushed out using fresh medium before being transferred to acoustically-transparent Lumox dishes (Sarstedt AG & Co. KG, Nümbrecht, Germany) that were sealed with water-impermeable acoustically transparent Sonolids, developed by the BUBBL group (Institute of Biomedical Engineering, Oxford University, UK)²⁸. One dish was filled with approximately 1500 spheroids in suspension in full medium. The cellular organization of the NIH/3T3 and 4T1 co-spheroids was verified by labeling NIH/3T3 cells with CellTrace™ Blue (excitation/emission maxima: 355/410 nm, Molecular Probes™, Thermo Fisher Scientific, Waltham, WA, USA) and labeling 4T1 cells with CellTrace™ Yellow (excitation/emission maxima 546/579 nm, Molecular Probes™) prior to spheroid formation.

Microbubbles

Biotinylated microbubbles were composed of DPPC (1,2-dipalmitoyl-sn-glycero-3-phosphocholine) (Avanti Polar Lipids, Alabaster, AL, USA) and DSPE-PEG₃₄₀₀-biotin (1,2-distearoyl-sn-glycero-3-phosphoethanol-amine-N-(biotinyl(polyethyleneglycol)-3400)) (Laysan Bio Inc, Arab, AL, USA) in a molar ratio of 85:15. Microbubbles without biotin were prepared as control samples (coadministration of microbubbles and liposomes) and were composed of DPPC (1,2-dipalmitoyl-sn-glycero-3-

phosphocholine) and DSPE-PEG₂₀₀₀ (1,2-distearoyl-sn-glycero-3-phosphoethanol-amine-N-[(polyethyleneglycol)2000] (Laysan Bio Inc, Arab, AL, USA) in the same molar ratio. The microbubbles were prepared as described previously^{10,12,29}. In short, appropriate amounts of the lipids in chloroform were mixed together in a round bottom flask. After evaporation of the chloroform using a rotavapor at 65°C, the lipid film was rehydrated in a preheated mixture of HEPES buffer (20 mM, pH 7.4), propylene glycol, and glycerol (ratio 7:2:1) resulting in a solution with a lipid concentration of 0.75 mg/mL. Aliquots of this lipid solution were transferred into 2.5 mL chromatography vials, of which the headspace was filled with C₄F₁₀ gas (F2 chemicals, Preston, UK). Finally, microbubbles were obtained by high speed shaking of the lipid solution for 15 s in a Capmix™ device (3 M-ESPE, Diegem, Belgium). The microbubbles were subsequently washed by centrifugation (750 g for 5 min at room temperature) using HEPES buffer. Afterwards, avidin (100 mg/mL, IBA GmbH, Göttingen, Germany) was added in excess and left to incubate for 5 min to couple to the biotin groups. The excess of avidin was again removed by 2 cycles of centrifugation and finally the avidinylated microbubbles were resuspended in HEPES buffer at a concentration of 10⁹ microbubbles/mL, as determined by the Coulter Counter (Multisizer 4, Beckman Coulter Life Sciences, Indianapolis, IN, USA).

Polystyrene beads

To evaluate the delivery of fluorescently stable model nanoparticles, yellow-green fluorescent carboxylate-modified polystyrene beads of 100 nm in size (excitation/emission: 505/515 nm, Molecular Probes™, Waltham, WA, USA) were coupled to the microbubble surface. To be able to attach the beads to the biotinylated microbubble surface, they were covalently coated with polyethylene glycol-biotin via amine-coupling as described before¹². To this end, 2 kDa biotin-PEG-amine (Creative PEGWorks, Winston Salem, NC, USA), N-(3-dimethylaminopropyl)-N'-ethylcarbodiimide hydrochloride (EDC) (Sigma Aldrich, Saint Louis, MO, USA), and N-hydroxysulfosuccinimide sodium salt (sulfo-NHS) (Sigma-Aldrich) were dissolved in HEPES Buffered Saline (HBS) (10 mM HEPES (Sigma-Aldrich), 150 mM NaCl (Sigma-Aldrich) containing 3.4 mM EDTA (Merck, Overijse, Belgium), 0.005% Tween 20 (Sigma-Aldrich) and adjusted to pH 8). The fluorescent beads were added to this mixture to give final concentrations of 4 mg/mL EDC, 1.13 mg/mL Sulfo-NHS, 10 mg/mL biotin-PEG-amine and 1% w/V beads. The mixture was rotated overnight at room temperature. The PEG-biotin modified beads were purified by ultracentrifugation (Beckman Coulter Life Sciences) at 234000 g for 45 min and resuspended in HBS to obtain a concentration of 2% w/V beads. The PEG-biotin coating was successful, since the zeta potential of the negatively charged beads increased after PEGylation, indicating partial shielding of the charge by the polymer coating, as measured with the Zetasizer Nano SZ (Malvern Panalytical). Finally, bead-loaded microbubbles were obtained by incubating 50 µL PEG-biotin modified beads with 1mL of the avidinylated microbubble suspension.

Liposomes

Regular liposomes consisted of DPPC (1,2-dipalmitoyl-sn-glycero-3-phosphocholine), DSPE-PEG₃₄₀₀-biotin (1,2-distearoyl-sn-glycero-3-phosphoethanol-amine-N-(biotinyl(polyethyleneglycol)-3400) and cholesterol (Avanti Polar Lipids) in a molar ratio of 55:5:40. Thermosensitive liposomes consisted of DPPC (1,2-dipalmitoyl-sn-glycero-3-phosphocholine), DSPE-PEG₃₄₀₀-biotin (1,2-distearoyl-sn-glycero-3-phosphoethanol-amine-N-(biotinyl(polyethyleneglycol)-3400) and MSPC (1-myristoyl-2-stearoyl-sn-glycero-3-phosphocholine) (Avanti Polar Lipids) in a molar ratio of 85:5:10. The composition of these liposomes were based on previous reports by Lentacker et al.³⁰ and Van Elk et al.³¹ for the regular (Doxil®-like) and thermosensitive (ThermoDOX®-like) liposomes respectively. 1 mol% of DiD (excitation/emission: 648/670 nm; Molecular Probes™, Thermo Fisher Scientific, Waltham, WA, USA) was added to the lipid mixture to prepare fluorescently labeled liposomes. Liposomes were prepared by transferring appropriate amounts of lipids dissolved in chloroform to a round bottom flask. Chloroform was removed via evaporation and HEPES buffer (20 mM, pH 7.4) was used to rehydrate the lipid film, resulting in a lipid concentration of 16 mg/mL. To reduce the liposome size, the lipid solution was sonicated in a bath sonicator (Branson Ultrasonics, Emerson, St. Louis, MO, USA) for 5 min. The final size was determined on a Zetasizer Nano SZ (Malvern Panalytical, Worcestershire, UK). Doxorubicin-loaded liposomes (DOX-liposomes) were prepared in the same way but were resuspended in (NH₄)₂SO₄ buffer (250 mM, pH 5.5) instead of in HEPES buffer, to enable active loading of doxorubicin into the liposomes³². Afterwards, the external (NH₄)₂SO₄ buffer was removed via ultracentrifugation (L8-70M ultracentrifuge equipped with a SW55Ti Rotor, Beckman Coulter Life Sciences) at 35 000 rpm for 1h at 25°C for the regular liposomes and via PD-10 columns (Sephadex G-25, GE Healthcare Life Sciences, Pittsburgh, PA, USA) in case of thermosensitive liposomes. Subsequently, 10 mg/mL of doxorubicin was added to the liposomes in a ratio of 1/10 and left to incorporate in the liposomes for 2h at 70°C in case of the regular liposomes and at 37°C in case of the thermosensitive liposomes. To remove the remaining free doxorubicin, another ultracentrifugation step (35 000 rpm, 1h, 25°C) was performed and the DOX-liposomes were finally resuspended in HEPES buffer. The doxorubicin concentration was determined by comparing the absorbance signal of the liposomes incubated with 10% Triton X-100 to release the doxorubicin from the DOX-liposomes at 450 nm, with the absorbance signals of a calibration curve of doxorubicin with known concentrations, in the presence of 10% Triton X-100 to account for background signal. Furthermore, a NanoSight LM10 system (Malvern Panalytical) was used to determine the concentration of liposomes, to allow the estimation of the amount of doxorubicin per liposome. Finally, 50 µL of both types of liposomes was added to 1 mL of the avidinylated microbubbles and allowed to incubate for 5 min. The coupling efficiency could be determined by measuring the free liposomal fraction remaining in the liposome-microbubble solution, by means of the NanoSight LM10. In the final experiment, we aimed to reduce the free liposomes in

the liposome-loaded microbubble samples. To this end, we added different amounts of liposomes to the microbubbles and determined the microbubble loading efficiency using flow cytometry since this method provided higher sensitivity.

Ultrasound treatment of tumor spheroids

Ultrasound radiations were performed at 37°C, in a water bath containing a rubber bottom layer to prevent reflections of the ultrasound beam. 100 µL of the bead-loaded or liposome-loaded microbubbles (LPS-MB + US) were added to the Lumox plates containing approximately 1000 spheroids in suspension. The Lumox dishes were completely filled with medium and sealed with Sonolids²⁸. The plates were radiated for 10 seconds using a Sonitron device (Sonitron 2000; Rich-Mar, Inola, OK, USA) with a 1 MHz center frequency, at 2 W/cm² (corresponding to 700 kPa PNP), 10% duty cycle and 2000 cycles per pulse and left to incubate for 4h before analysis. The ultrasound parameters correspond to optimal acoustic settings required for sonoprinting, as defined in our previous work^{12,13}. The control samples included a “coadministration” sample, where 5 µL of beads or liposomes and 100 µL of non-biotinylated microbubbles were transferred to the Lumox plates together and radiated with ultrasound in the same way as the coupled sample and a “bead only” or “liposomes only” sample, where 5 µL of beads/liposomes was added but no ultrasound exposure occurred. In the doxorubicin-containing experiments an additional “doxorubicin only” sample was included, in which the same concentration of free doxorubicin was added without ultrasound exposure. The amount of free doxorubicin to be added was calculated based on the encapsulation efficiency of doxorubicin in the liposomes, to make sure exactly the same amount was used in the different samples. For these experiments, the excess of free doxorubicin or doxorubicin-filled liposomes with or without microbubbles was removed via a centrifugation step 15 min after treatment (5 min at 1100 rpm) to prevent delayed doxorubicin leakage. Finally, all samples were exposed to a heating step of 15 min at 42°C in which the thermosensitive liposomes released their doxorubicin content, and left to incubate for 24h before analysis.

Flow cytometry

To be able to analyze the delivery of liposomes to spheroid cells with flow cytometry, the spheroids had to be disintegrated to a single cell suspension. Therefore, the spheroids were incubated with 1 mL of Trypsin - EDTA (Gibco™) for 5 min, after which they were further disintegrated into single cells by mechanical disruption using a 21G needle (BD, Franklin Lakes, NJ, USA) attached to a 1 mL syringe (BD). Afterwards, the trypsin was neutralized and the single cell suspensions were and finally resuspended in flow buffer (i.e. PBS-/- (Gibco™) supplemented with 1% of BSA (Sigma Aldrich) and 0.5% of NaN₃ (Sigma Aldrich). Flow cytometric data were acquired using a CytoFLEX (Beckman Coulter Life Sciences,

Indianapolis, IN, USA) and analyzed using FlowJo™ software. Single cell gating was performed to remove the signal from remaining doublets and triplets.

The loading capacity of microbubbles using fluorescently loaded liposomes could also be detected with flow cytometry. To this end, the liposomes were added to the microbubbles in the specified ratios and left to incubate for 5 min before measuring on flow cytometry. Like for spheroid cells, flow cytometric data of microbubbles were acquired using a CytoFLEX (Beckman Coulter Life Sciences, Indianapolis, IN, USA) and analyzed using FlowJo™ software. Gating was performed to selectively measure the microbubble bound liposomal fluorescence.

Confocal microscopy

All confocal microscopy images were performed on a C1-si confocal microscope (Nikon, Amsterdam, The Netherlands) equipped with a 60× water immersion objective (NIR Apo, Nikon) and a 10x air objective (Plan Apo, Nikon). A 405 nm laser was used to visualize Hoechst 33342 or DAPI associated with the cellular nuclei; a 488 nm laser was used to excite doxorubicin autofluorescence, while the emitted signal was detected over the TRITC emission window. Finally, a 637 nm laser was used to visualize DiD, present in the liposomal bilayer. Confocal imaging was performed on 10 µm cryosections, as well as on intact spheroids. When imaging living spheroids, the spheroids were transferred to glass-bottom microscopy grade dishes (CELLview™ cell culture dishes, Greiner Bio-One, Kremsmünster, Austria). Optical cross sections of the spheroids were made with a 1 µm increment and used to produce Z stacks of the spheroid volume. To determine the radial fluorescence plot profile in a single cross section, the 'Radial Profile' plug-in for the image analysis software ImageJ (NIH, MD, USA) was used.

Histology

Paraffin-embedded sections

The spheroids were fixated in 4% paraformaldehyde (VWR, Radnor, PA, USA), dehydrated through an ethanol concentration gradient and embedded in paraffin. Sections of 5 µm thickness were cut (Cut4060; Slee Medical, Mainz, Germany) and deparaffinized. Histological staining was done using a standard protocol for hematoxylin-eosin to evaluate cell morphology. The presence of extracellular matrix in the spheroids was tested by collagen I staining (1:150, R1086, Acris Antibodies GmbH, Herford, Germany). In short, enzymatic digestion of the sections was achieved by incubation with 1 mg/mL pepsin at 37°C for 30 min. Subsequently 2 h of incubation with a monoclonal mouse anti-collagen I antibody was performed after pretreatment with 3% H₂O₂ for 10 min and blocking with BSA and 4% normal rabbit serum in PBS. Afterwards streptavidin-peroxidase was left to incubate for 30 min before a secondary antibody (biotinylated swine anti rabbit, 1:200, E2431, Dako, Agilent Technologies,

Santa Clara, CA, USA) was added. Finally, the sections were incubated with DAB for 10 min and counterstained with hematoxylin. Imaging was subsequently done on an Olympus BX51 microscope.

Cryosections

Spheroids were fixated in 4% PFA for 30 min prior to embedding in Tissue-Tek® O.C.T. (Sakura Finetek USA Inc, Torrance, CA, USA). The spheroids were subsequently snap frozen with liquid nitrogen and 10 µm sections were cut using a Cryotome® FSE (Thermo Fisher Scientific, Cheshire, UK) and allowed to adhere to Superfrost microscopic glass slides (Menzel-Gläser, Braunschweig, Germany). The sections were air dried for 20 min before adding DAPI-containing mounting medium. The cryosections were visualized under confocal microscopy as described before.

Toxicity assays

To estimate general spheroid cell viability, a CellTiter-Glo® 3D Cell Viability Assay (Promega Corporation, Madison, WI, USA), was performed on spheroids that were treated as described above, since this assay is optimally adapted for the evaluation of toxicity in 3D cell cultures³³. For this, the spheroids were transferred to low adherent gyratory shaker flasks and placed on a shaker plate at 37°C and 70 rpm, to remain in 3D culture until analysis. After 72h, the spheroids were incubated with the CellTiter-Glo® 3D reagent and analyzed as described by the manufacturer, using a GloMax® 96 Microplate luminometer (Promega). Cell viability was normalized against untreated spheroids.

To selectively evaluate the viability of tumor cells within mono- and co-cultures, a firefly luciferase assay was performed on spheroids containing Luciferase positive 4T1 cells. Similarly as in the CellTiter-Glo® assay, spheroids were kept in 3D cultures after treatment by gyratory shaking for 72h. Afterwards, the spheroids were incubated with a 5x dilution of Luciferase Cell Culture Lysis 5X Reagent (Promega) for 20 min. After lysis, the spheroid cell content was transferred to a 96 white flat bottom well plate (Corning Incorporated, Corning, NY, USA) and the remaining luciferase activity of the 4T1 cells was determined using the Luciferase Assay System from Promega. Therefore, a CLARIOstar luminometer (BMG Labtech, Cary, NC, USA) with injection system was programmed to perform a 2 second delay, follow by a 10 second read-out, as instructed by the manufacturer.

Incucyte® live cell analysis

Spheroid morphology was evaluated using the IncuCyte® 3S Live Cell Analysis System ((Essen Bioscience, Hertfordshire, UK) over 72h. For this, a single spheroid was handpicked under a ... microscope and transferred to a Corning® 96-well Clear Round Bottom Ultra-Low Attachment Microplate (Corning Incorporated, Corning, NY, USA) containing 100 µL full medium. The plate was inserted in the Incucyte 3S live-cell analysis system (Essen Bioscience, Hertfordshire, UK) and images at 10x magnification were taken every 1,5 to 2 hours for 72h.

Statistical analysis

All experiments were performed independently on different days with a minimum of 3 replicates. Statistical analysis was performed using one-way ANOVA analysis with a Bonferroni's multiple comparison test, as calculated by GraphPad Prism 6 (GraphPad software, San Diego, CA, USA) and expressed as the mean \pm standard deviation.

Results

Multicellular spheroids as a 3D tumor model

Spheroids were generated using an agarose-based microwell array platform, as developed by Vrij et al²⁶, in which single cells assemble into multicellular spheroid cultures of approximately 100 to 150 μm in size within 48h (Fig 1A). This system yields a large amount of uniformly sized spheroids that are able to interact freely with the microbubbles in suspension. Based on the earlier work of Priwitaningrum et al.²⁷ we included 4T1 breast cancer monospheroids and cospheroids consisting of 4T1 cells and NIH/3T3 fibroblasts (in a 1:5 ratio) in this study. When fibroblasts are added, a more biologically relevant spheroid model arises due to the formation of an extracellular matrix which resembles the stroma found in various breast cancer phenotypes²⁷. It has been shown before that the presence of an extracellular matrix can hinder nanoparticle penetration and renders nanoparticle-based treatments less effective as a consequence^{20–22,25,34}. The comparison between mono- and cospheroids will therefore indicate if the extracellular matrix affects the sonoprinting efficiency and how it influences nanoparticle deposition and drug release.

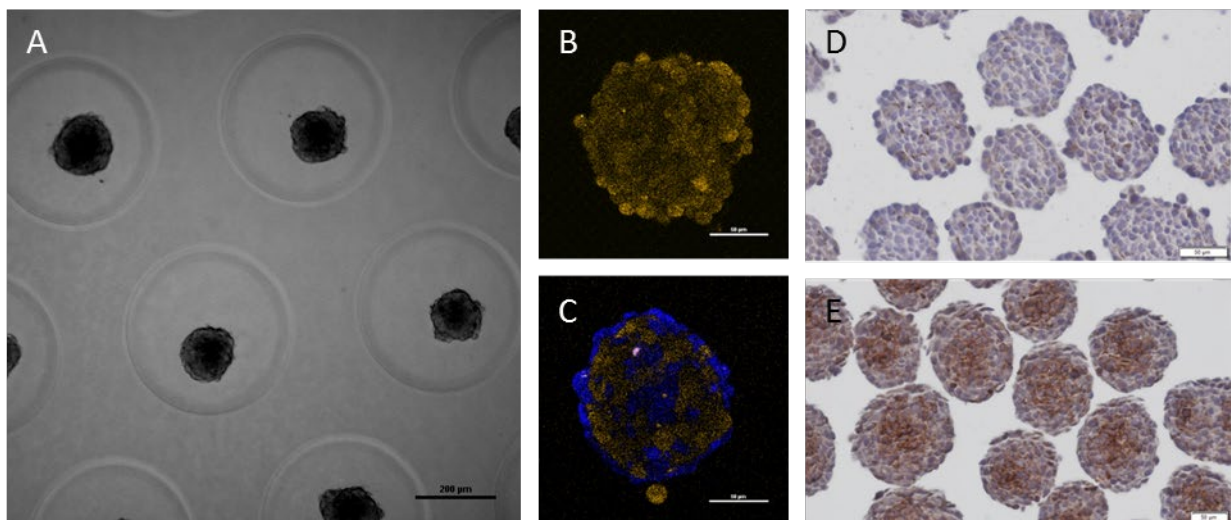


Figure 1: **Mono- and cospheroids as 3D cell culture model.** (A) Bright-field image of cospheroids grown in a microwell array platform. The scale bar represents 200 μm . (B) Confocal image of a monospheroid consisting of 4T1 tumor cells, labeled with CellTrace™ Yellow (cross section at approx. 30 μm from the top). (C) Confocal image of a cospheroid consisting of 4T1 tumor cells and NIH/3T3 fibroblast cells in a 1:5 ratio, differentially labeled with CellTrace™ Yellow and CellTrace™ Blue respectively (cross section at 25-30 μm from the top). (D) Collagen-1 staining on paraffin sections of monospheroids showing little to no

collagen formation within the monospheroids. **(E)** Collagen-1 staining on paraffin sections of cospheroids indicating the presence of an extracellular matrix in these cospheroids. **(B-E)** The scale bar represents 50 μm .

To investigate the cellular organization of the spheroids, NIH/3T3 and 4T1 cells were labeled with two different CellTrace™ dyes prior to spheroid formation and subsequently imaged with confocal microscopy. Figure 1B and C show the localization of 4T1 cells (yellow) and NIH/3T3 cells (blue) in mono- and cospheroids respectively. Due to a difference in cellular density the NIH/3T3 cells cluster among themselves, which is why they accumulate within the center and on the outer part of the spheroids^{25,27}. To confirm that the inclusion of NIH/3T3 fibroblasts resulted in the formation of an extracellular matrix, we investigated the presence of collagen-1 in both spheroid types. Collagen-1 staining was performed on paraffin sections of both mono- and cospheroids, as seen in figure 1D and 1E. The images show that collagen-1 (brown color) is abundantly present in the co-spheroids (fig. 1E) while almost no collagen-1 signal can be seen in the monospheroids (fig. 1D). Additionally, the collagen-1 is predominantly found in the center of the cospheroids which is in accordance with the confocal images showing that a high concentration of NIH/3T3 fibroblasts was found in the center of the cospheroids.

Sonoprinting enhances the delivery of nanoparticles to tumor spheroids

In previous work, we have shown that the ultrasound-triggered delivery of nanoparticles was significantly increased when loading these nanoparticles on the microbubble shell, through a mechanism called sonoprinting. To determine if this phenomenon also applies to 3D cultures and in the absence of ultrasound-reflecting membranes, we loaded two types of nanoparticles onto the microbubbles using a biotin-avidin-biotin link. Figure 2 shows confocal images of fluorescent bead-loaded (Fig. 2A) and DiI-labeled liposome-loaded microbubbles (Fig. 2B) and the corresponding size distribution, as determined by Coulter Counter (Fig. 2C). The size of the microbubbles ranged between 1 and 10 μm , with an average size of 2.5 μm for unloaded microbubbles and 2.6 μm and 2.8 μm for liposome-loaded and bead-loaded microbubbles respectively. The size and pdl of the different nanoparticles used in this study can be found in supplementary table 1.

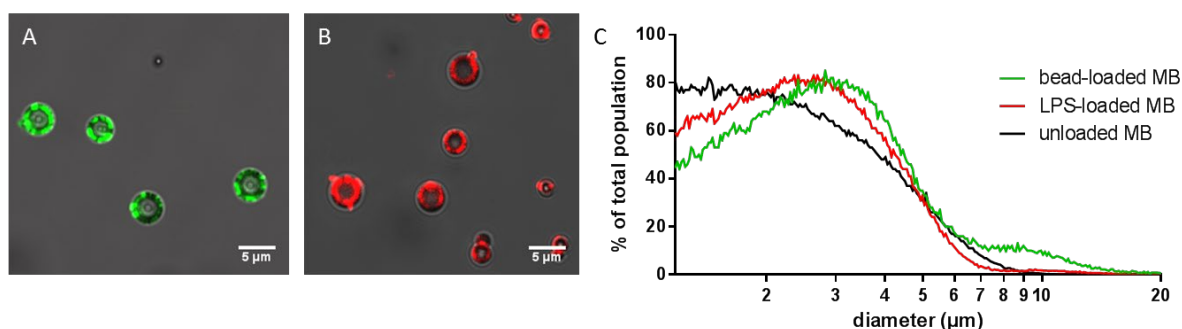


Figure 2. **Characterization of nanoparticle-loaded microbubbles.** (A-B) Confocal image of microbubbles loaded with (A) yellow-green fluorescent 100 nm polystyrene beads (green) and (B) DiD-labeled liposomes (red). The scale bar represents 5 μm . (C) Size distribution of unloaded (black), bead-loaded (green) and liposome-loaded (red) microbubbles, as determined via Coulter Counter.

Two nanoparticle types were utilized to evaluate sonoprinting on 3D tumor spheroids. At first instance, fluorescent polystyrene beads were used as model nanoparticles as they are inert and as such any possible leaching of the dye from the nanoparticles can be avoided. Green fluorescent beads were surface-modified with PEG-biotin, coupled onto the microbubbles and added to a suspension of 4T1 monospheroids before ultrasound treatment (1 MHz, 700 kPa, 1000 cycles). Flow cytometry was used to quantitatively evaluate the delivery of these beads to spheroid-derived single cells 4h after treatment. The delivery efficiency of the microbubble-coupled beads exposed to ultrasound, was compared to the delivery efficiency of the fluorescent beads alone and a coadministration sample in which beads and microbubbles were not coupled but exposed to the same ultrasound conditions, as shown in figure 3A (black bars). These results clearly show that microbubble loading drastically improves the delivery efficiency of the fluorescent beads compared to the beads-only sample and the coadministration sample. This confirms that sonoprinting is not an artefact caused by the rather stiff membrane on which cells grow in 2D cultures, but also occurs on 3D cultures in suspension. A similar trend was obtained in the case of cospheroids, consisting of 4T1 tumor cells and NIH/3T3 fibroblasts (figure 3B, black bars) indicating that the presence of the extracellular matrix is not influencing the sonoprinting process.

The same experiments were repeated with fluorescently (DiD) labeled liposomes, as they are a highly versatile and flexible drug carriers which are able to encapsulate several small molecular weights drugs (chemotherapeutics, corticosteroids), as well as complex larger biological drugs (mRNA, siRNA)^{2,35–37}. Figure 3A and B (grey bars) show that the delivery efficiency of liposomes was very similar to that of the polystyrene beads.

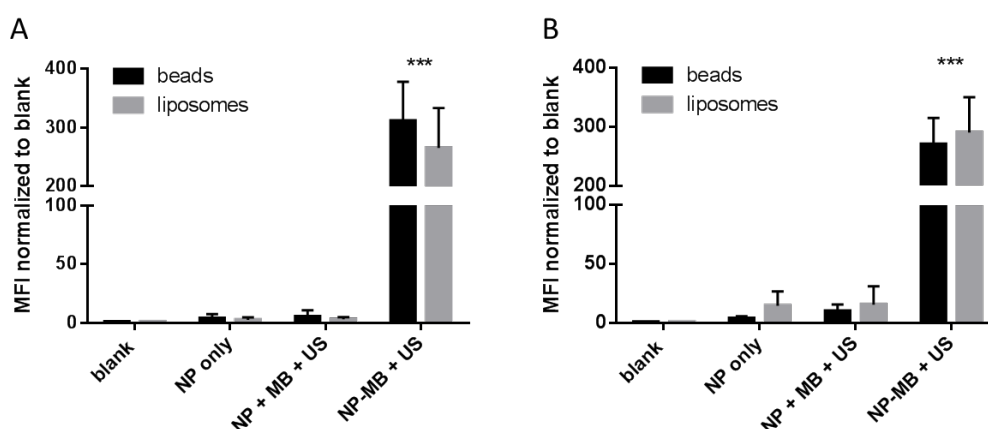


Figure 3: **Sonoprinting on 3D spheroids of tumor cells only (A) and tumor cells co-cultured with fibroblasts (B).** Normalized (to blank) mean intensity fluorescence (MFI) of liposomal and bead-derived fluorescence on 4T1 and NIH/3T3 spheroid cells determined using flow cytometry. NP = nanoparticles; MB = microbubbles; US = ultrasound; NP + MB + US = nanoparticles and microbubbles coadministered before ultrasound radiation; NP-MB + US = nanoparticles loaded onto the microbubbles and exposed to ultrasound. Significance levels are determined using a Bonferroni multiple comparison test: *** represents $P < 0.001$.

However, since single cell suspensions are required for flow cytometric analysis, these results cannot reveal the exact location of the liposome-containing cells within the spheroids. Consequently, we further investigated the specific location of the fluorescently-labeled liposomes within the tumor spheroids with confocal imaging, as shown in figure 4. Therefore, we made individual cross-sections (fig 4G) over the entire depth of the spheroid with a 1 μm increment, which allowed us to make a reconstructed volume view (z-stack) of the entire spheroid (fig 4F). In correspondence with the flow cytometry results, the reconstructed z-stacks in figure 4A-D indicate that microbubble loading and ultrasound treatment can significantly enhance the nanoparticle delivery to the tumor spheroids (Fig 4D). This is in sharp contrast to the liposomes alone and the coadministration sample where only a limited delivery of the fluorescent nanoparticles (Fig 4B&C) was seen. The individual cross-sections at increasing depth of the spheroid treated with liposome-loaded microbubbles and ultrasound (depicted in 4D) are shown in figure 4E, which illustrates that liposome penetration is limited to the outer layers of the tumor spheroid. Due to the spheroid size (150 μm in average), it is impossible to visualize the deeper lying inner part of the tumor spheroid with confocal imaging, as light penetration is typically limited to a few tens of microns^{25,38,39}. Figure 4H shows a radial fluorescence profile plot from the cross-section at 40 μm in figure 4E (as illustrated in figure 4G). The plot indicates that the Hoechst nuclear staining was visible at a further distance from the spheroid surface than the DiD-labeled liposomes, despite the fact that the 637nm laser light, used to excite the DiD liposomes, has a better tissue penetration than the 405nm laser light, exciting the Hoechst nuclear stain⁴⁰. This confirms that the liposomes are indeed printed rather superficially and that the loss in liposomal fluorescence is not due a loss in fluorescence signal because of light scattering. Together, these results indicate that sonoprinting results in an increased liposomal delivery to the tumor spheroids but with a limited penetration depth.

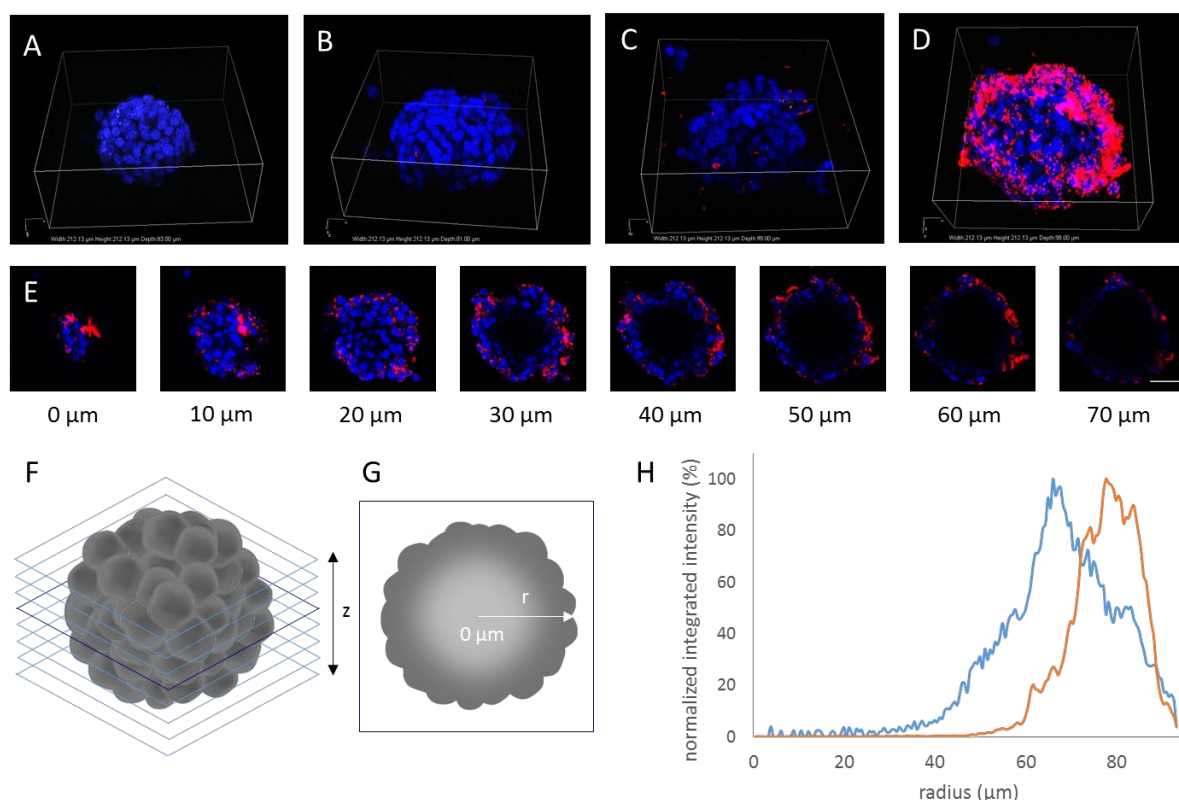


Figure 4: **Sonoprinting on 4T1 tumor monospheroids.** Blue = Hoechst 33342 nuclear stain, red = liposomes (DiD). **(A-D)** Maximum intensity projections of Z stacks taken from **(A)** an untreated spheroid, **(B)** a spheroid exposed to only DiD-labeled liposomes, **(C)** a spheroid exposed to DiD-labeled liposomes coadministered with microbubbles and exposed to ultrasound and **(D)** a spheroid exposed to DiD-labeled liposomes coupled onto microbubbles and exposed to ultrasound. The dimensions of the white boxes are: 212 μm x 212 μm x 90 μm . **(E)** Individual cross sections of the spheroid in **(D)** at increasing depth. The scale bar represents 50 μm . **(F)** The maximum intensity projection of the spheroid is composed from stacks of cross sections in the z direction. **(G)** The radial profile plot is created by measuring the fluorescence profile over radius r over the entire spheroid. **(H)** Radial profile plot of the nuclear stain (blue) and the liposomal stain (red) from the spheroid center (0 μm) to the edges.

Sonoprinting can enhance the distribution of chemotherapeutics into tumor spheroids

To have an idea whether the printed liposomes can be used as a drug reservoirs and can leak small molecular weight drugs to enhance their distribution within the tumor spheroid, we included the potent chemotherapeutic drug doxorubicin (DOX) in the liposomes. First, doxorubicin-loaded liposomes (DOX-liposomes) were biophysically characterized and the doxorubicin loading was determined. To this end, both the concentration of doxorubicin and the concentration of liposomes in the DOX-liposome sample were measured, as described in materials and methods. From this, the amount of doxorubicin per liposome was calculated and was found to be $3.1 \cdot 10^{-10}$ μg doxorubicin/liposome on average, which is comparable to the doxorubicin content of Doxil®, a clinically approved doxorubicin-containing liposomal formulation⁴¹. The active loading of doxorubicin into the liposomes increased the liposomal size to approximately 200 nm (supplementary table 1).

After coupling the liposomes to the microbubbles, both the microbubble concentration as the concentration of unbound liposomes could be determined, as described in materials and methods. From these, we were able to calculate the doxorubicin loading of the microbubbles which corresponded to $1,6 \cdot 10^{-7}$ μg doxorubicin per microbubble.

Doxorubicin is a small, hydrophobic drug that can easily penetrate intercellular junctions, cell membranes and nuclear membranes where it can subsequently intercalate in the DNA and exert its cytotoxic function. Since doxorubicin has auto-fluorescent properties, both the drug-derived fluorescence and the liposome-derived fluorescence on the spheroids could be individually measured, as illustrated in figure 5. From the flow cytometry scatter plot in figure 5A, it becomes clear that only the monospheroids that were exposed to DOX-liposome loaded microbubbles and ultrasound (dark blue dots) showed a higher delivery of both liposomal (y-axis) and doxorubicin fluorescence (x-axis) after 24h. Within this population, there is a clear gradient in cellular fluorescence, most likely corresponding to the cellular localization of the single cells within the spheroid (i.e. cells located in the outer spheroid layers show a higher uptake of fluorescently DOX-liposomes). From these scatter plots, it also becomes evident that there is a strong correlation between the liposomal and the doxorubicin delivery, which suggests that the drug was still contained in the liposomes and that intact DOX-liposomes were printed on the tumor spheroid. Free doxorubicin penetrates the tumor spheroid cells very well, while the control samples (liposomes only and co-administration of liposomes and microbubbles) completely overlap and show only a modest increase in both liposomal and doxorubicin fluorescence. An identical trend was seen in cospheroids, as evidenced in supplementary figure 1A.

DOX-liposomes are known to be extremely stable and can resist premature degradation up to 2 weeks *in vitro*^{32,41-43}. To verify whether DOX can be released from the printed liposomes and is able to distribute within the tumor, we prepared thermosensitive DOX-liposomes resembling clinically approved ThermoDOX^{®31}. These DOX-liposomes contain a lysolipid (MSPC), that enables the disintegration of the liposomal structure after the application of a simple heating step around its T_m i.e. at mild hyperthermia^{44,45}. We have used these thermosensitive DOX-liposomes along with the regular DOX-liposomes and shortly heated the culture medium with the tumor spheroids to 42°C. This heating step was done after the removal of any remaining DOX-liposomes not associated with the spheroids using a centrifugation step after treatment for all the different experimental groups. The flow cytometry scatter plots from these thermosensitive DOX-liposomes 24h after treatment can be found in figure 5B (monospheroids) and supplementary figure 1B (cospheroids). In contrast to the data shown in fig. 5A and suppl. fig. 1A, the correlation between the liposomal and the DOX fluorescence in the sonoprinted group (dark blue dots) was less prominent, indicating that part of the doxorubicin was indeed able to leak out of the liposomes. We also found that the cells derived from the tumor spheroids

treated with free DOX-liposomes (dark green) or the co-administration sample (light green) have shifted towards a higher cellular delivery of both doxorubicin and liposomal DiD. This is presumably due to the improved penetration of the lipophilic DiD dye from the liposomal fragments and dequenching of the released doxorubicin in these samples⁴⁶. However, coupling the thermosensitive DOX-liposomes onto microbubbles before ultrasound radiation still results in much higher delivery rates.

To confirm these results and to have a clear view on the exact localization of the liposomes and the doxorubicin within the tumor spheroids we prepared spheroid cryosections of 10 μm and studied them with confocal microscopy. In this experiment we compared the localization of liposomes (red fluorescence) and doxorubicin (orange fluorescence) within the spheroids when regular (fig. 5C) or thermosensitive (fig. 5D) DOX-liposomes were sonoprinted. In case of the regular DOX-liposomes, it is clear from fig. 5C that the liposomal signal overlaps with the autofluorescence from doxorubicin and that both are limited to the outer layers of the spheroids, which was expected due to the slow release kinetics of Doxil[®] liposomes^{32,41–43}. In contrast, the cryosections of spheroids printed with the thermosensitive formulation (figure 5D) confirm that doxorubicin was able to leak out of the liposomes immediately and penetrate through the complete spheroid volume after a short heating step and subsequently intercalated in the cell nuclei. Since limited liposomal penetration was already present in monospheroids, it was not surprising that also co-cultures of tumor cells and fibroblasts, showed similar results, as seen in supplementary figure 1C&D.

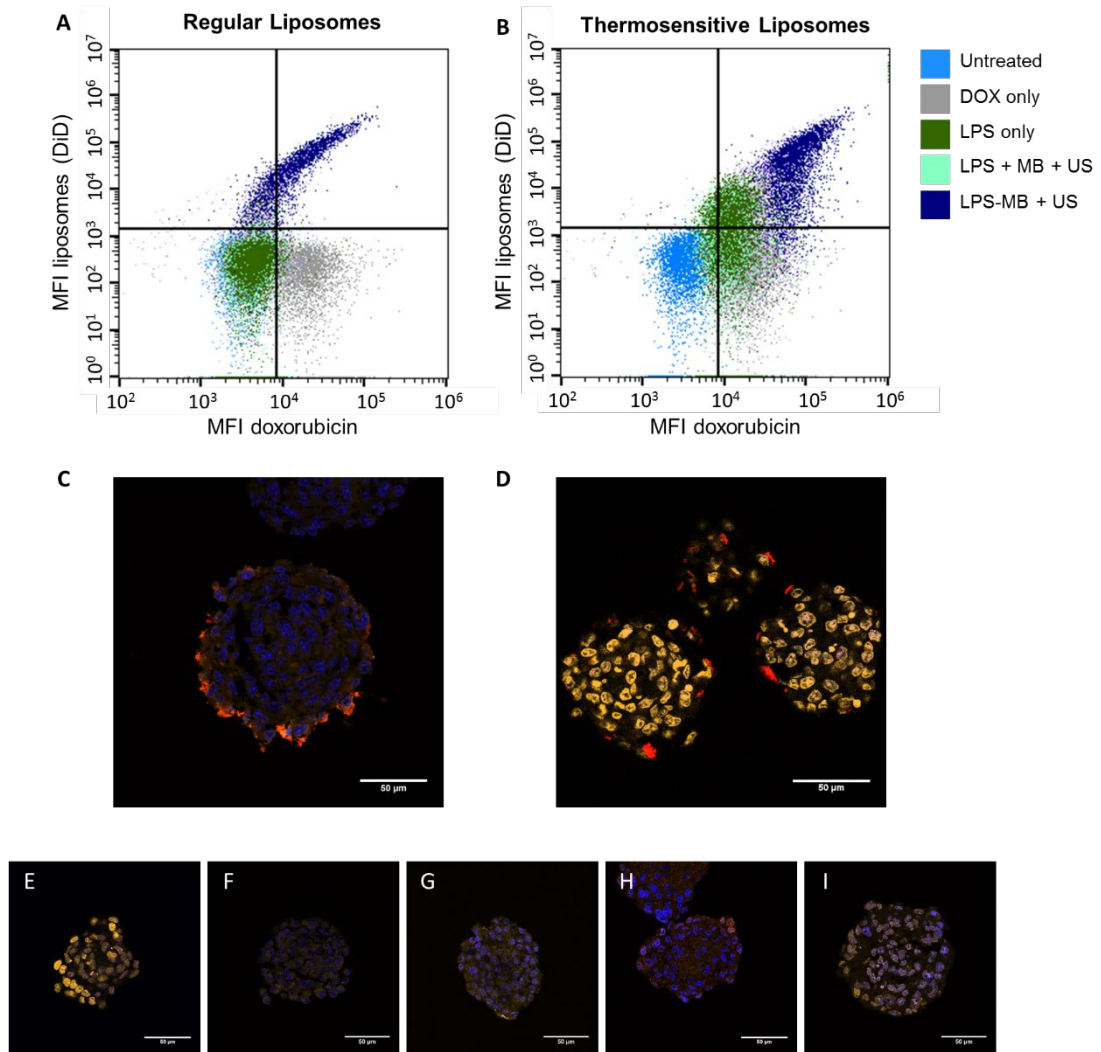


Figure 5: **Localization of doxorubicin within a multicellular monospheroid 24h after sonoprinting followed by a heating step. (A&B)** Flow intensity scatter plots of the cellular delivery of doxorubicin (orange fluorescence, horizontal axis) and **(A)** regular and **(B)** thermosensitive liposomes (red fluorescence, vertical axis). DOX = doxorubicin; LPS = DOX-liposomes; MB = microbubbles; US = ultrasound; LPS + MB + US = DOX-liposomes and microbubbles coadministered before ultrasound radiation; LPS-MB + US = DOX-liposomes loaded onto the microbubbles and exposed to ultrasound. **(C-I)** 10 μm cryosections of a monospheroid treated with **(C)** regular or **(D)** thermosensitive DOX-liposomes coupled onto microbubbles and exposed to ultrasound; **(E)** DOX only; **(F)** regular or **(G)** thermosensitive DOX-liposomes only; **(H)** regular or **(I)** thermosensitive DOX-liposomes coadministered with microbubbles and exposed to ultrasound. Blue = Hoechst 33342 nuclear stain, orange = doxorubicin, red = liposomes (DiD). The scale bar indicates 50 μm .

The therapeutic efficacy of liposomal doxorubicin is enhanced by sonoprinting

To validate whether the local accumulation of doxorubicin leads to a higher therapeutic effect, the spheroid morphology was followed over 72h after treatment. Figure 6 and Supplementary Movie 1 and 2 show typical examples of the difference in spheroid morphology over time when spheroids were untreated or treated with ultrasound and microbubbles carrying regular DOX-liposomes. Both types of untreated spheroids grow in size over time (fig 6B&D), in contrast with treated monospheroids that

desintegrate (fig 6A), while treated cospheroids mainly shed cell fragments (fig 6C). This difference might be due to the extracellular matrix components in cospheroids that hold the spheroid mass together.

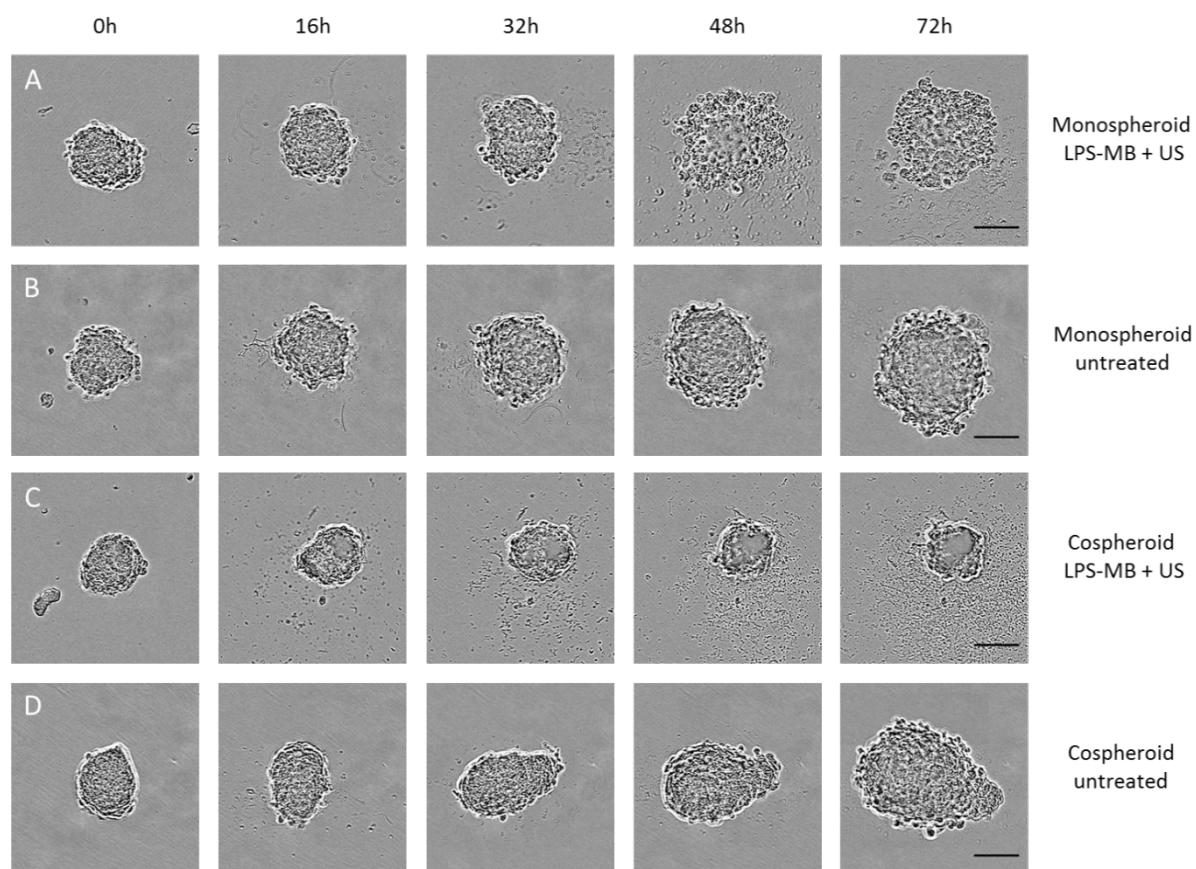


Figure 6: **Spheroid morphology followed over 72h after treatment.** (A) Monospheroids treated with regular DOX-liposomes coupled onto microbubbles and exposed to ultrasound and (B) untreated monospheroids. (C) Cospheroids treated with regular liposomes coupled onto microbubbles and exposed to ultrasound and (D) untreated cospheroids. The scale bar indicates 50 μ m.

Based on the time profile captured in figure 6, the total cell viability was assessed using a CellTiter-Glo® 3D Cell Viability Assay 72h after treatment of the monospheroids (Fig 7A) and cospheroids (Fig 7B).

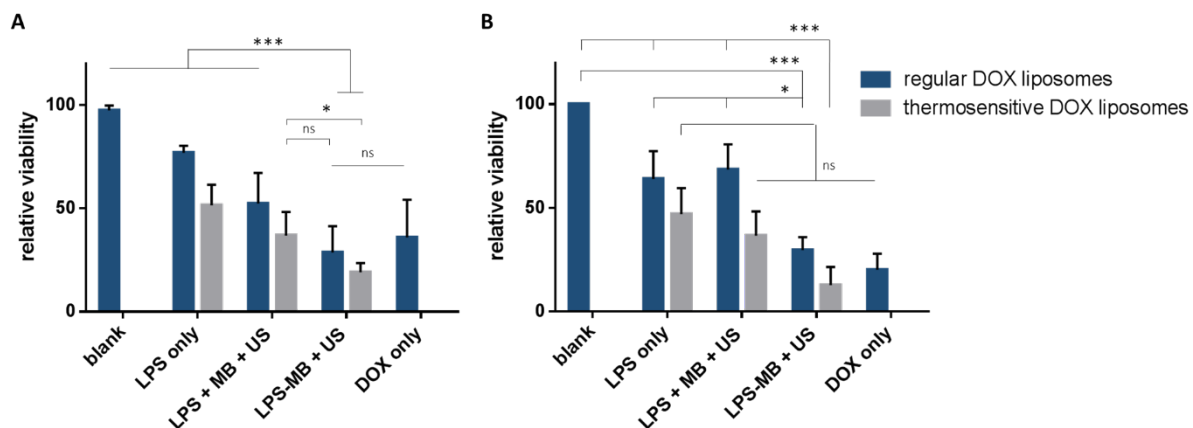


Figure 7: **Total cell viability of tumor spheroids 72h after treatment of (A) monospheroids and (B) cospheroids** using a CellTiter-Glo® 3D Viability Assay. DOX = doxorubicin; LPS = DOX-liposomes; MB = microbubbles; US = ultrasound; LPS + MB + US = DOX-liposomes and microbubbles coadministered before ultrasound radiation; LPS-MB + US = DOX-liposomes loaded onto the microbubbles and exposed to ultrasound. Significance levels are determined using a Bonferroni multiple comparison test: ns for $P > 0.05$, * for $P < 0.05$, ** for $P < 0.01$, *** for $P < 0.001$.

In general, the thermosensitive DOX-liposomes were slightly more toxic compared to the regular liposome samples, although not always statistically significant. Sonoprinting of DOX-liposome-loaded microbubbles resulted in a significantly reduced cell viability compared to the control samples (co-administration or free DOX-liposomes), and this for regular as well as for thermosensitive liposomes. This indicates that the cell killing efficiency of microbubbles carrying either regular or thermosensitive DOX-liposomes is similar after 72h, even though we did not detect any free doxorubicin in the cryosections of tumor spheroids sonoprinted with regular DOX-LPS 24h after treatment (figure 5). Therefore, additional cryosections were made of monospheroids at different time points after treatment with DOX-liposome-loaded microbubbles and ultrasound, which are depicted in figure 8. Doxorubicin leakage from the thermosensitive liposomal patches occurred within 4h while DOX release from the printed regular liposomes could only be detected after 48h.

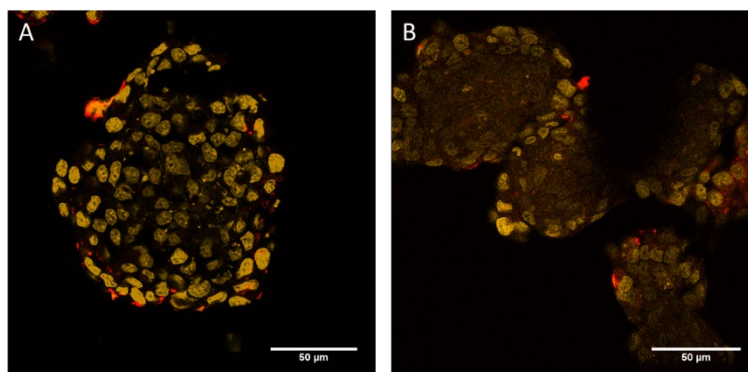


Figure 8: **Doxorubicin release from patches of (A) thermosensitive DOX-liposomes coupled onto microbubbles and exposed to ultrasound and (B) regular DOX-liposomes coupled onto microbubbles and exposed to ultrasound.** Confocal images of 10

μm cryosections of monospheroids 4h and 48h after treatment respectively. Orange = doxorubicin, red = liposomes (DiD). The scale bar indicates 50 μm .

It was reported before that the presence of fibroblasts in cancerous tissues can have a pro-carcinogenic effect due to the formation of a dense matrix structure acting as a physical barrier for penetration, rendering anti-cancer treatments less efficient^{20–22,34}. Therefore, an additional toxicity test was performed to evaluate the protective effect of the NIH/3T3-derived matrix on the 4T1 tumor cell viability. For this assay, we prepared mono and cospheroids with luciferase positive 4T1 cells and exposed them to the same treatments as in the first toxicity experiment. 72h after treatment, a firefly luciferase assay was performed to selectively evaluate the viability of the 4T1 tumor cells in mono- and cospheroids (Fig 9). The results indicate that the 4T1 cells in the cospheroids were less efficiently killed and confirms that the presence of NIH/3T3 fibroblasts can indeed protect the tumor cells from the cytostatic effects of doxorubicin. However, in case the tumor spheroids were treated with DOX-liposome-loaded microbubbles (both regular and thermosensitive) and ultrasound, we were not able to detect a significant difference between mono- and cospheroids. Under these conditions, the treatment was equally effective in killing the tumor cells within the 3D culture.

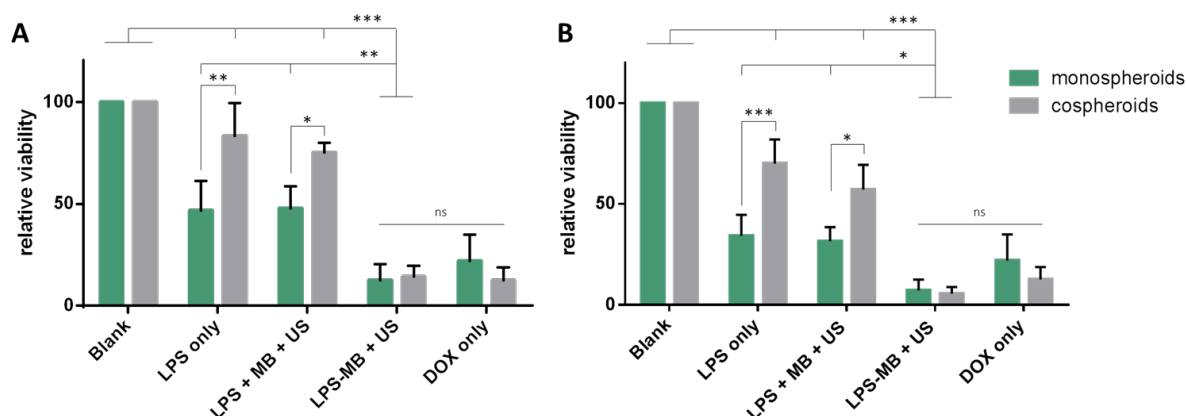


Figure 9: **Selective tumor cell viability after treatment** with (A) regular DOX-liposome samples and (B) thermosensitive DOX-liposome samples using a Luciferase-based viability assay. DOX = doxorubicin; LPS = DOX-liposomes; MB = microbubbles; US = ultrasound; LPS + MB + US = DOX-liposomes and microbubbles coadministered before ultrasound radiation; LPS-MB + US = DOX-liposomes loaded onto the microbubbles and exposed to ultrasound. Significance levels are determined using a Bonferroni multiple comparison test: ns for P > 0.05, * for P < 0.05, ** for P < 0.01, *** for P < 0.001.

Only microbubble-loaded liposomes are responsible for the sonoprinting effect and associated drug release.

In a final experiment, we optimized the liposome-coupled microbubble formulation in such a way that the amount of free liposomes in the formulation was minimized while maintaining the majority of liposomes on the microbubbles. For this, we measured the liposomal load of the microbubbles with

flow cytometry while the liposome:microbubble ratio decreased (supplementary figure 2). From these results, it became clear that a 5 fold reduction in liposome:microbubble ratio only slightly reduced microbubble loading to 80% of the original microbubble formulation. Finally we compared sonoprinting efficiency of the two microbubble formulations by measuring the uptake of fluorescently labeled liposomes in monospheroids with flow cytometry (figure 10A). The results show that there is no significant difference in the improvement of liposomal delivery to the spheroid cells, indicating that there is no added benefit of having a free liposomal fraction in the coupled sample. These results are confirmed by the toxicity data in figure 10B, where we noticed no significant difference in toxicity after 72h although 5 times less DOX-liposomes were added to the microbubble sample.

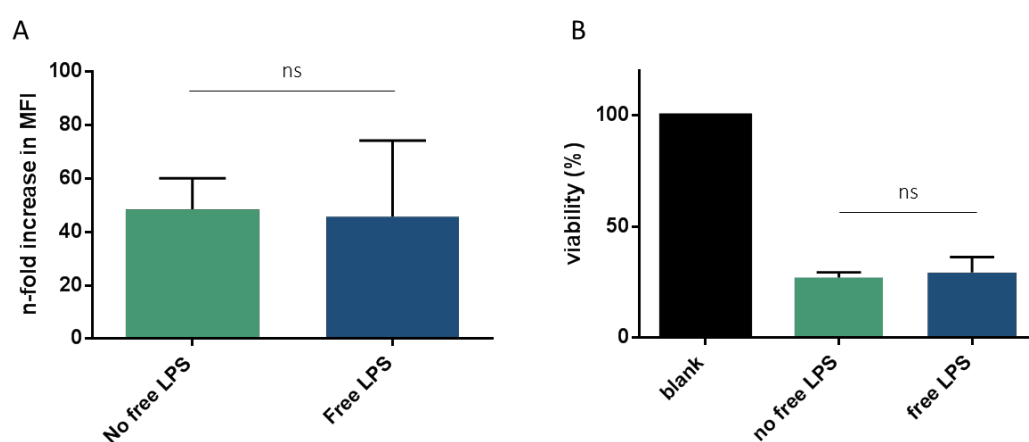


Figure 10: **The effect of the free liposomal fraction.** **(A)** Relative increase in liposomal MFI of monospheroid cells treated with DOX-liposomes coupled onto microbubbles and exposed to ultrasound as compared to monospheroid cells treated with free DOX-liposomes, determined by flow cytometry. **(B)** Total cell viability after 72h as determined using a CellTiter-Glo® 3D assay. DOX = doxorubicin; LPS = DOX-liposomes; MB = microbubbles; US = ultrasound; LPS-MB + US = DOX-liposomes loaded onto the microbubbles and exposed to ultrasound. Significance levels are determined using a Bonferroni multiple comparison test: ns for $P > 0.05$.

Discussion

In this study, we were able to show that the loading of nanoparticles onto the microbubbles surface led to an enhanced ultrasound-triggered local delivery of these liposomes on the outer layers of 3D tumor spheroids in suspension. We proved that very similar delivery rates were obtained for polystyrene beads and liposomes, indicating that the increased delivery was not caused by liposomal fragmentation or leaching of the liposomal dye. This was not surprising, as Ying et al.⁴⁷ have shown before that intact liposomes are released from the microbubble shell upon ultrasound radiation. Moreover, as earlier published by Lea-Banks et al., the density of nanoparticles can influence their ultrasound-mediated tissue penetration drastically⁴⁸. Since the density of polystyrene (1040 kg/m³) closely resembles the density of liposomes (997 kg/m³), their penetration depth within tumor spheroids is expected to be comparable as well.

The resulting patches closely resemble the sonoprinted patches that we described earlier in 2D cell cultures¹². This implies that the ultrasound-assisted sonoprinting of nanoparticles is not caused by acoustic artefacts arising from the rigid membrane on which cells are grown in a 2D monolayer cell culture. Our results also prove that a significant enhancement in the delivery of drug-loaded nanoparticles can be obtained in a more complex biological setting i.e. in avascular tumor nodules containing multiple cell layers.

Since sonoprinting is based on the biophysical interaction of nanoparticle-loaded microbubbles with cells or tissues, it is not surprising that nanoparticle delivery is limited to the first few cell layers of the tumor spheroids. Previous studies have shown that liposomes can only penetrate limited distances (maximally 40-50 μm from the nearest blood vessel), depending on size and charge^{27,49-52}. Moreover, in a previous study, we have shown that nanoparticles can remain (partly) attached to microbubble shell fragments upon delivery to the cell surface, contributing to the restricted penetration¹³. However, sonoprinting can result in the formation of a local depot system, which provides a high drug concentration in close proximity of the target tissue, while evading the need for a high systemic drug concentration. For potent chemotherapeutics with the right physicochemical properties to penetrate tissues, but that suffer from dose limitation due to off-target effects (e.g. doxorubicin), this approach could be highly promising^{30,53}. Even more so, since we showed that the total doxorubicin concentration could be lowered since uncoupled liposomes do not add to the therapeutic effects (figure 10). However, in case the drug carriers are filled with more sensitive therapeutics, such as gene products, their limited penetration will form a pitfall since these products will be degraded before entering the deeper target cells⁵⁴⁻⁵⁶.

Even though mono- and cospheroids vary significantly in composition and penetration barrier, we only noticed minor differences in liposomal penetration in this study. In contrast, a recent study by Priwitaningrum et al. on similar spheroids showed a strong difference in nanoparticle penetration within both 3D cultures²⁷. This discrepancy might be due to their use of higher nanoparticle concentrations favoring diffusion, smaller nanoparticle sizes and their serum-free conditions, preventing the formation of a protein corona. Since the bulky doxorubicin-filled liposomes did not manage to infiltrate monospheroids of tumor cells, it comes as no surprise that a similar pattern was observed for more dense co-cultures of tumor cells and fibroblasts. Vice versa, the ideal physicochemical properties of free doxorubicin allowed it to penetrate both mono- and cospheroids. The selective toxicity assay (figure 9) revealed the pro-carcinogenic effect of cancer-associated fibroblasts, as the control samples were more effective in monospheroids than in cospheroids. Nevertheless, the viability of both the mono- and cospheroids could be efficiently reduced with DOX-liposome-loaded microbubbles and ultrasound and no significant difference between both tumor models was seen.

It seems counterintuitive that a comparable tumor killing efficiency was achieved in the samples treated with regular DOX-liposome, where the doxorubicin remained encapsulated inside the liposomes after 24h, and those treated with thermosensitive DOX-liposomes, where an immediate release of doxorubicin was induced by a short heating step (figure 7). However, the spheroid morphology data (figure 6 and supplementary movies 1&2) and the doxorubicin leakage as seen in figure 8, suggest that the main toxic action of regular DOX-liposomes takes place at a later time point, suggesting that the doxorubicin within the regular DOX-liposomes was finally able to leak out and induce equal cell killing after 72h. The mechanisms behind the drug release of comparable commercial doxorubicin-based liposomal formulations, such as Doxil®, are not yet fully elucidated^{41,57,58}. It was reported that these types of liposomes have extremely slow leakage kinetics that cannot justify the mechanism-of-action^{32,42}. As a possible explanation, it was suggested that the uptake of the nanomedicine by a selected population of tumor cells or macrophages, which would result in apoptosis of these cells and a subsequent release of the free doxorubicin within their cytosol^{32,42,57}. Another option is that since doxorubicin is encapsulated through remote loading in the presence of ammonium sulfate or similar, an enhanced ammonia concentration at the tumor site, through an activation of the glutaminolysis pathway, may reverse this process and release the doxorubicin as a result⁴¹. Which one, if any, of these mechanisms is responsible for the equal tumor cell killing efficiency of this formulation, and whether or not these mechanisms are all accurately represented in this tumor model, remains an open question.

The total doxorubicin concentration using in this work equaled 4.2 μg doxorubicin per mL spheroid-containing medium. Since a single injection of Doxil[®] results in an average plasma concentration of approximately 25 $\mu\text{g}/\text{mL}$, with respect to doxorubicin^{59,60}, our local deposition of DOX-liposomes could provide effective tumor cell killing while using a 5x lower total doxorubicin concentration. Even more so, since we showed that the total doxorubicin concentration could be lowered to 0.8 $\mu\text{g}/\text{mL}$, as uncoupled liposomes do not add to the therapeutic effects (figure 10). It is furthermore highly beneficial to load this lower concentration of liposomes onto microbubbles, since unresponsive microbubbles will be rapidly cleared from the circulation, while severe side-effects can arise in patients treated with Doxil, due to liposomal accumulations the small capillaries of the extremities (hand-foot syndrome). The microbubble concentration used in this study approximated 2×10^7 microbubbles/mL. To achieve the same doxorubicin concentration as used here, 10^{11} microbubbles should be administered to a patient with a standard blood volume of 5L. The recommended dose of clinically approved contrast agent Definity[®] equals 10^{10} microbubbles for a patient of 80 kg³⁰, however it has been demonstrated that Definity[®] doses that are 1000 times higher are well tolerated in primates^{61,62}. Therefore, it would be feasible to achieve clinical effects using this microbubble formulation.

Even though multicellular tumor spheroids have a higher cellular complexity than monolayer cultures and are therefore a better representative of the *in vivo* situation, there are evidently some limitations to its predictability as well. Since microbubbles are too large to extravasate through endothelial gaps, they will remain inside the vascular compartment in the clinical situation. As a result, the presence of blood flow and an endothelial cell layer would normally permit only a brief and indirect contact between the target tissue and the drug-carrying microbubbles. However, when using targeted microbubbles, it is possible to attain a local accumulation of the microbubbles and elongate the contact time, as to resemble the conditions present in this study. Targeting can be achieved through the incorporation of tumor vasculature-specific ligands on the microbubble shell^{63–65}, as well as through physical forces such as the application of an external magnetic field^{66,67} and ultrasound-induced radiation forces^{68–70}. Adding targeting moieties to the liposomes could also affect the liposomal uptake through receptor-mediated internalization⁷¹. Secondly, the lack of an endothelial cell layer does not allow to investigate its effect on the drug delivery events described here. Nevertheless, it has been extensively shown that ultrasound-driven microbubbles can lead to the disruption of the vascular wall through the formation of pores in the endothelial cell membranes and the opening of gap junctions^{52,72,73}. Even the highly impermeable vascular wall that makes up the blood-brain-barrier can be opened in this way^{74,75}. However, unlike in the brain parenchyma, where any cell is within 2 or 3 cells away from a blood vessel⁷⁴, peripheral tumors can form avascular regions where viable cells can be as far as 200 μm away from the nearest capillaries^{76,77}. An appropriate treatment of such tissues

requires a therapy that can reach the deeper laying layers as well as the cells closest to the vasculature and overcome the enhanced stromal content. Therefore, 3D models remain suitable *in vitro* models.

Future mechanistic studies could be performed on more advanced 3D cultures, for example in tumor spheroids encompassing blood vessel-like structures for a better representation of the vascular barrier^{78,79}. Alternatively, tumor spheroids grown in microfluidic chips could be employed as they mimic the blood flow around the tissue more accurately^{80,81}. In this way, more valuable *in vitro* data that allows to study microbubble-tissue interactions in close detail, could be obtained leading to a better future understanding and predictability of ultrasound-mediated therapeutic applications.

Conclusion

Nanoparticle-loaded microbubbles exposed to ultrasound are able to increase the delivery and therapeutic efficacy of drug-containing nanoparticles in 3D mono- and cospheroids. This ultrasound-triggered delivery can be attributed to sonoprinting, which only occurs when nanoparticles are loaded onto the microbubble surface. Sonoprinting results in the deposition of nanoparticle patches onto the outer layers of the tumor spheroid. As such, a local reservoir is formed, from where small molecular weight drugs can leak out and distribute deeper into the tumor tissue. This could be a mechanism to enhance the intratumoral delivery of different types of nanoparticles, as it is based on a physical trigger and does not rely on the enhanced permeation and retention effect.

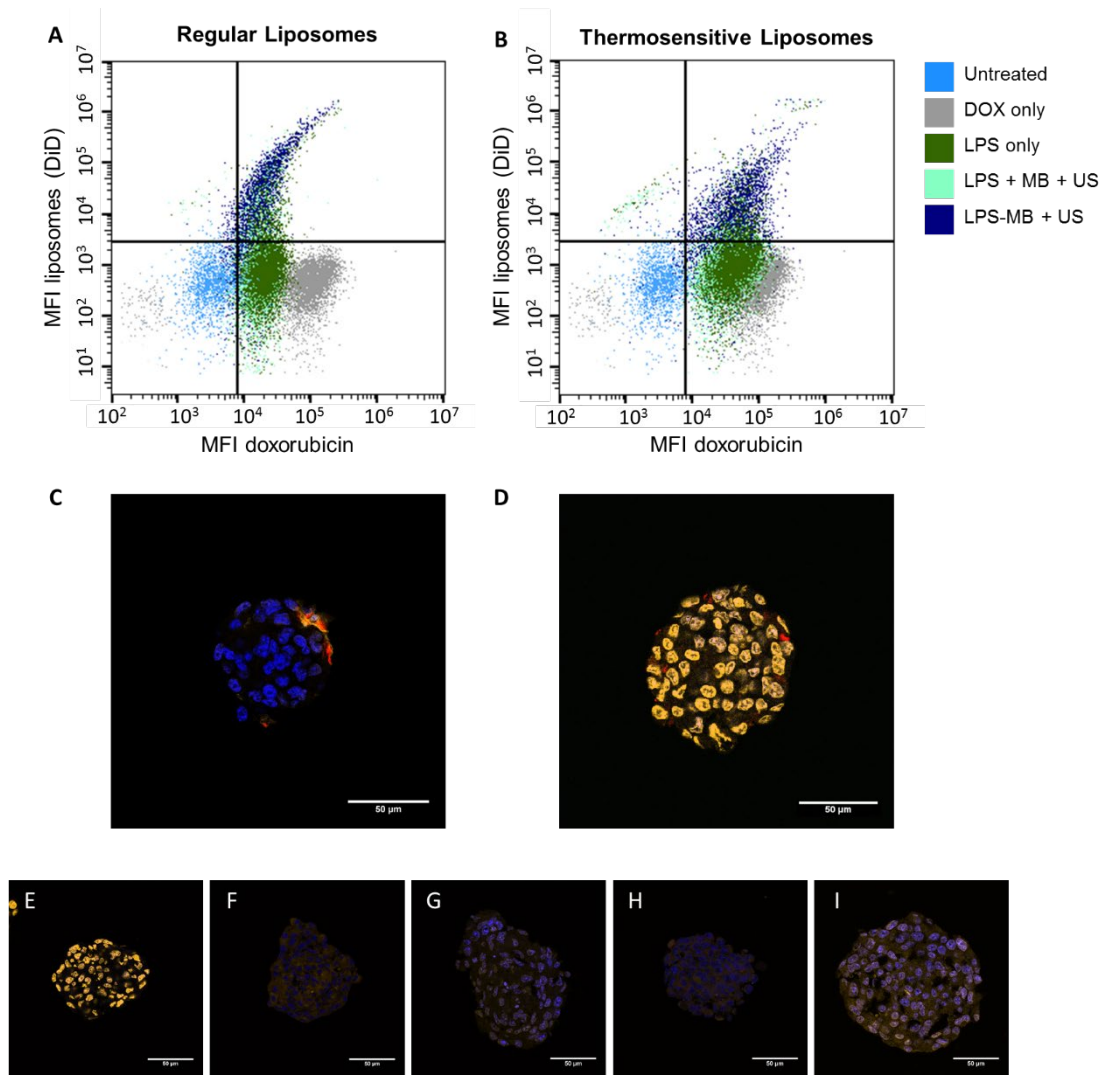
Acknowledgements

Silke Roovers is a doctoral fellow of the Special Research Fund in Flanders Belgium (BOF-Vlaanderen). The project was also funded through NanoCOMIT, an SBO project granted by the Institute for the Promotion of Innovation through Science and Technology in Flanders, Belgium (IWT-Vlaanderen, project number 140061). The support of all of these institutes is gratefully acknowledged.

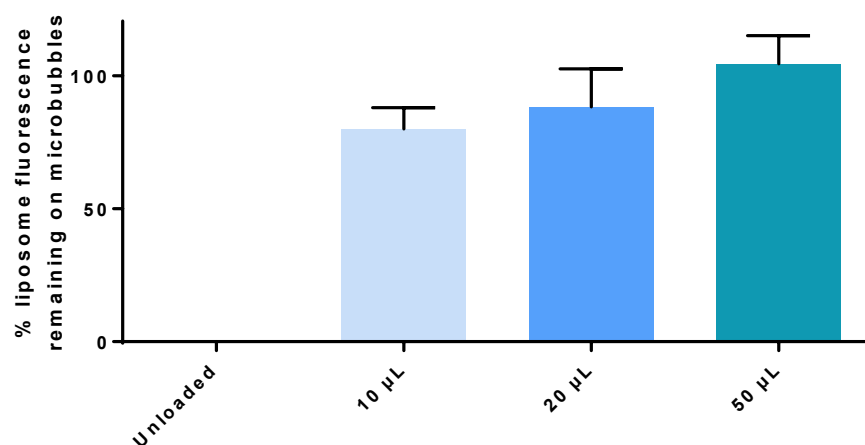
Supplementary data

Supplementary Table 1: average size and Pdl of different liposomes, as determined by DLS.

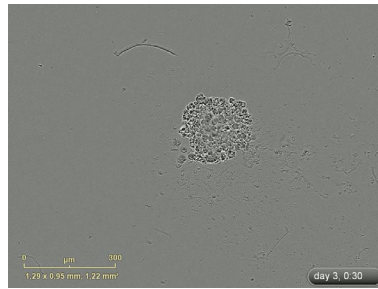
	AVERAGE SIZE (NM)	PDI
REGULAR + DID	119,0	0,316
REGULAR + DOX	199,5	0,189
REGULAR + DOX + DID	210,5	0,238
THERMO + DOX	201,7	0,326
THERMO + DOX + DID	213,6	0,314



Supplementary Figure 1: **Localization of doxorubicin within a multicellular cospheroid 24h after sonoprinting followed by a heating step.** (A&B) Flow intensity scatter plots of the cellular delivery of doxorubicin (orange fluorescence, horizontal axis) and (A) regular and (B) thermosensitive liposomes (red fluorescence, vertical axis). DOX = doxorubicin; LPS = liposomes; MB = microbubbles; US = ultrasound; LPS + MB + US = liposomes and microbubbles coadministered before ultrasound radiation; LPS-MB + US = liposomes loaded onto the microbubbles and exposed to ultrasound. (C-I) 10 μ m cryosections of a cospheroid treated with (C) regular or (D) thermosensitive DOX-liposomes coupled onto microbubbles and exposed to ultrasound; (E) DOX only; (F) regular or (G) thermosensitive DOX-liposomes only; (H) regular or (I) thermosensitive DOX-liposomes coadministered with microbubbles and exposed to ultrasound. Blue = Hoechst 33342 nuclear stain, orange = doxorubicin, red = liposomes (DiD). The scale bar indicates 50 μ m.



Supplementary Figure 2: **Optimization of the liposome to microbubble ratio.** Percentage of liposomal mean fluorescence intensity remaining on the microbubbles when different amounts of DiD-labeled liposomes were coupled onto 1 mL of microbubbles. 50 µL of liposomes was used as a reference (corresponding with 100% liposomal fluorescence).



Supplementary Movie 1: Monospheroid treated with regular DOX-liposomes coupled onto microbubbles and exposed to ultrasound and followed over 72h after treatment. The full scale bar indicates 300 μm .



Supplementary Movie 2: Cospheroid treated with regular DOX-liposomes coupled onto microbubbles and exposed to ultrasound and followed over 72h after treatment. The full scale bar indicates 300 μm .

References

1. Maeda, H. Macromolecular therapeutics in cancer treatment: The EPR effect and beyond. *Journal of Controlled Release* **164**, 138–144 (2012).
2. Lammers, T., Kiessling, F., Hennink, W. E. & Storm, G. Drug targeting to tumors: Principles, pitfalls and (pre-) clinical progress. *Journal of Controlled Release* **161**, 175–187 (2012).
3. Boissenot, T., Bordat, A., Fattal, E. & Tsapis, N. Ultrasound-triggered drug delivery for cancer treatment using drug delivery systems: From theoretical considerations to practical applications. *Journal of Controlled Release* **241**, (2016).
4. Wilhelm, S. *et al.* Analysis of nanoparticle delivery to tumours. *Nature Reviews Materials* **1**, (2016).
5. Dreher, M. R. *et al.* Tumor vascular permeability, accumulation, and penetration of macromolecular drug carriers. *J. Natl. Cancer Inst.* **98**, 335–344 (2006).
6. Maeda, H. Toward a full understanding of the EPR effect in primary and metastatic tumors as well as issues related to its heterogeneity. *Advanced Drug Delivery Reviews* **91**, 3–6 (2015).
7. Hernot, S. & Klivanov, A. L. Microbubbles in ultrasound-triggered drug and gene delivery. *Advanced Drug Delivery Reviews* **60**, 1153–1166 (2008).
8. Stewart, M. P., Langer, R. & Jensen, K. F. Intracellular delivery by membrane disruption: Mechanisms, strategies, and concepts. *Chemical Reviews* **118**, 7409–7531 (2018).
9. Roovers, S. *et al.* The role of ultrasound-driven microbubble dynamics in drug delivery: from microbubble fundamentals to clinical translation. *Langmuir* [acs.langmuir.8b03779](https://doi.org/10.1021/acs.langmuir.8b03779) (2019). doi:10.1021/acs.langmuir.8b03779
10. De Cock, I. *et al.* Ultrasound and microbubble mediated drug delivery: acoustic pressure as determinant for uptake via membrane pores or endocytosis. *J. Control. Release* **197**, (2015).
11. Helfield, B., Chen, X., Watkins, S. C. & Villanueva, F. S. Biophysical insight into mechanisms of sonoporation. *Proc. Natl. Acad. Sci.* **113**, (2016).
12. De Cock, I., Lajoinie, G., Versluis, M., De Smedt, S. C. & Lentacker, I. Sonoprinting and the importance of microbubble loading for the ultrasound mediated cellular delivery of nanoparticles. *Biomaterials* **83**, 294–307 (2016).
13. De Cock, I. Unravelling microbubble-cell interactions and drug delivery mechanisms in ultrasound-guided therapy. (2016).

14. Vos, H. J., Dollet, B., Bosch, J. G., Versluis, M. & de Jong, N. Nonspherical Vibrations of Microbubbles in Contact with a Wall-A Pilot Study at Low Mechanical Index. *Ultrasound Med. Biol.* **34**, 685–688 (2008).
15. Lajoinie, G. *et al.* Non-spherical oscillations drive the lipid shedding of microbubbles near a boundary.
16. Helfield, B. L., Leung, B. Y. C. & Goertz, D. E. The effect of boundary proximity on the response of individual ultrasound contrast agent microbubbles. *Phys. Med. Biol.* **59**, 1721–1745 (2014).
17. Mehta, G., Hsiao, A. Y., Ingram, M., Luker, G. D. & Takayama, S. Opportunities and challenges for use of tumor spheroids as models to test drug delivery and efficacy. *J. Control. Release* **164**, 192–204 (2012).
18. Chandrasekaran, S. Gather Round: In vitro tumor spheroids as improved models of in vivo tumors. *J. Bioeng. Biomed. Sci.* **02**, (2012).
19. Junttila, M. R. & De Sauvage, F. J. Influence of tumour micro-environment heterogeneity on therapeutic response. *Nature* **501**, 346–354 (2013).
20. Prakash, J. & Pinzani, M. Fibroblasts and extracellular matrix: Targeting and therapeutic tools in fibrosis and cancer. *Advanced Drug Delivery Reviews* **121**, 1–2 (2017).
21. Choi, S. Y. C. *et al.* Lessons from patient-derived xenografts for better in vitro modeling of human cancer. *Adv. Drug Deliv. Rev.* **79**, 222–237 (2014).
22. Leong, D. T. & Ng, K. W. Probing the relevance of 3D cancer models in nanomedicine research. *Adv. Drug Deliv. Rev.* **79**, 95–106 (2014).
23. Xu, X., Farach-Carson, M. C. & Jia, X. Three-dimensional in vitro tumor models for cancer research and drug evaluation. *Biotechnol. Adv.* **32**, 1256–1268 (2014).
24. Alemany-Ribes, M. & Semino, C. E. Bioengineering 3D environments for cancer models. *Adv. Drug Deliv. Rev.* **79**, 40–49 (2014).
25. Pampaloni, F., Ansari, N. & Stelzer, E. H. K. High-resolution deep imaging of live cellular spheroids with light-sheet-based fluorescence microscopy. *Cell Tissue Res.* **352**, 161–177 (2013).
26. Vrij, E. *et al.* Directed Assembly and Development of Material-Free Tissues with Complex Architectures. *Adv. Mater.* **28**, 4032–4039 (2016).

27. Priwitaningrum, D. L. *et al.* Tumor stroma-containing 3D spheroid arrays: A tool to study nanoparticle penetration. *J. Control. Release* **244**, 257–268 (2016).
28. Carugo, D., Owen, J., Crake, C., Lee, J. Y. & Stride, E. Biologically and Acoustically Compatible Chamber for Studying Ultrasound-Mediated Delivery of Therapeutic Compounds. *Ultrasound Med. Biol.* **41**, 1927–1937 (2015).
29. De Temmerman, M. L. *et al.* mRNA-Lipoplex loaded microbubble contrast agents for ultrasound-assisted transfection of dendritic cells. *Biomaterials* **32**, 9128–9135 (2011).
30. Lentacker, I., Geers, B., Demeester, J., De Smedt, S. C. & Sanders, N. N. Design and evaluation of doxorubicin-containing microbubbles for ultrasound-triggered doxorubicin delivery: Cytotoxicity and mechanisms involved. *Mol. Ther.* **18**, 101–108 (2010).
31. van Elk, M. *et al.* Alginate Microspheres Containing Temperature Sensitive Liposomes (TSL) for MR-Guided Embolization and Triggered Release of Doxorubicin. *PLoS One* **10**, e0141626 (2015).
32. Barenholz, Y. Doxil® - The first FDA-approved nano-drug: Lessons learned. *J. Control. Release* **160**, 117–134 (2012).
33. Zanoni, M. *et al.* 3D tumor spheroid models for in vitro therapeutic screening: A systematic approach to enhance the biological relevance of data obtained. *Sci. Rep.* (2016). doi:10.1038/srep19103
34. Alemany-Ribes, M. & Semino, C. E. Bioengineering 3D environments for cancer models. *Advanced Drug Delivery Reviews* **79**, 40–49 (2014).
35. Lombardo, D., Calandra, P., Barreca, D., Magazù, S. & Kiselev, M. Soft Interaction in Liposome Nanocarriers for Therapeutic Drug Delivery. *Nanomaterials* (2016). doi:10.3390/nano6070125
36. Pattni, B. S., Chupin, V. V. & Torchilin, V. P. New Developments in Liposomal Drug Delivery. *Chem. Rev.* (2015). doi:10.1021/acs.chemrev.5b00046
37. Xing, H., Hwang, K. & Lu, Y. Recent developments of liposomes as nanocarriers for theranostic applications. *Theranostics* (2016). doi:10.7150/thno.15464
38. Centonze, V. E. & White, J. G. Multiphoton excitation provides optical sections from deeper within scattering specimens than confocal imaging. *Biophys. J.* (1998). doi:10.1016/S0006-3495(98)77643-X
39. Vinci, M. *et al.* Advances in establishment and analysis of three-dimensional tumor spheroid-

- based functional assays for target validation and drug evaluation. *BMC Biol.* (2012). doi:10.1186/1741-7007-10-29
40. Ruggiero, E., Alonso-De Castro, S., Habtemariam, A. & Salassa, L. Upconverting nanoparticles for the near infrared photoactivation of transition metal complexes: New opportunities and challenges in medicinal inorganic photochemistry. *Dalt. Trans.* (2016). doi:10.1039/c6dt01428c
 41. Silverman, L. & Barenholz, Y. In vitro experiments showing enhanced release of doxorubicin from Doxil® in the presence of ammonia may explain drug release at tumor site. *Nanomedicine Nanotechnology, Biol. Med.* **11**, 1841–1850 (2015).
 42. Russell, L. M., Hultz, M. & Searson, P. C. Leakage kinetics of the liposomal chemotherapeutic agent Doxil: The role of dissolution, protonation, and passive transport, and implications for mechanism of action. *J. Control. Release* **269**, 171–176 (2018).
 43. Jiang, W., Lionberger, R. & Yu, L. X. In vitro and in vivo characterizations of PEGylated liposomal doxorubicin. *Bioanalysis* (2011). doi:10.4155/bio.10.204
 44. Landon, C. D. Nanoscale Drug Delivery and Hyperthermia: The Materials Design and Preclinical and Clinical Testing of Low Temperature-Sensitive Liposomes Used in Combination with Mild Hyperthermia in the Treatment of Local Cancer. *Open Nanomed. J.* (2011). doi:10.2174/1875933501103010038
 45. Needham, D., Anyarambhatla, G., Kong, G. & Dewhirst, M. W. A new temperature-sensitive liposome for use with mild hyperthermia: Characterization and testing in a human tumor xenograft model. *Cancer Res.* (2000).
 46. Wu, N. Z. *et al.* Simultaneous measurement of liposome extravasation and content release in tumors. *Microcirculation* (1997). doi:10.3109/10739689709148320
 47. Luan, Y. *et al.* Acoustical Properties of Individual Liposome-Loaded Microbubbles. *Ultrasound Med. Biol.* **38**, 2174–2185 (2012).
 48. Lea-Banks, H., Teo, B., Stride, E. & Coussios, C. C. The effect of particle density on ultrasound-mediated transport of nanoparticles. *Phys. Med. Biol.* **61**, 7906–7918 (2016).
 49. Grainger, S. J. *et al.* Pulsed ultrasound enhances nanoparticle penetration into breast cancer spheroids. *Mol. Pharm.* **7**, 2006–2019 (2010).
 50. Albanese, A., Tang, P. S. & Chan, W. C. W. The Effect of Nanoparticle Size, Shape, and Surface

- Chemistry on Biological Systems. *Annu. Rev. Biomed. Eng.* **14**, 1–16 (2012).
51. Jain, R. K. & Stylianopoulos, T. Delivering nanomedicine to solid tumors. *Nature Reviews Clinical Oncology* **7**, 653–664 (2010).
 52. Theek, B. *et al.* Sonoporation enhances liposome accumulation and penetration in tumors with low EPR. *J. Control. Release* **231**, 77–85 (2016).
 53. Zheng, J. H., Chen, C.-T., Au, J. L. S. & Wientjes, M. G. Time-and concentration-dependent penetration of doxorubicin in prostate tumors. *AAPS PharmSci* **3**, 69–77 (2001).
 54. Raemdonck, K., Vandenbroucke, R. E., Demeester, J., Sanders, N. N. & De Smedt, S. C. Maintaining the silence: reflections on long-term RNAi. *Drug Discovery Today* **13**, 917–931 (2008).
 55. Riley, M. & Vermeris, W. Recent Advances in Nanomaterials for Gene Delivery—A Review. *Nanomaterials* **7**, 94 (2017).
 56. Delalande, A., Kotopoulis, S., Postema, M., Midoux, P. & Pichon, C. Sonoporation: Mechanistic insights and ongoing challenges for gene transfer. *Gene* **525**, 191–199 (2013).
 57. Storm, G., Steerenberg, P. A., Emmen, F., van Borssum Waalkes, M. & Crommelin, D. J. A. Release of doxorubicin from peritoneal macrophages exposed in vivo to doxorubicin-containing liposomes. *BBA - Gen. Subj.* **965**, 136–145 (1988).
 58. Seynhaeve, A. L. B., Dicheva, B. M., Hoving, S., Koning, G. A. & Ten Hagen, T. L. M. Intact Doxil is taken up intracellularly and released doxorubicin sequesters in the lysosome: Evaluated by in vitro/in vivo live cell imaging. *J. Control. Release* **172**, 330–340 (2013).
 59. Gabizon, A., Shmeeda, H. & Barenholz, Y. Pharmacokinetics of pegylated liposomal doxorubicin: Review of animal and human studies. *Clinical Pharmacokinetics* (2003). doi:10.2165/00003088-200342050-00002
 60. Ren, S. *et al.* Comparison of pharmacokinetics, tissue distribution and pharmacodynamics of liposomal and free doxorubicin in tumour-bearing mice following intratumoral injection. *J. Pharm. Pharmacol.* (2014). doi:10.1111/jphp.12257
 61. Karshafian, R., Bevan, P. D., Williams, R., Samac, S. & Burns, P. N. Sonoporation by Ultrasound-Activated Microbubble Contrast Agents: Effect of Acoustic Exposure Parameters on Cell Membrane Permeability and Cell Viability. *Ultrasound Med. Biol.* **35**, 847–860 (2009).
 62. Unger, E. C. *et al.* Therapeutic applications of lipid-coated microbubbles. *Adv. Drug Deliv. Rev.*

(2004). doi:10.1016/j.addr.2003.12.006

63. Ibsen, S. *et al.* The behavior of lipid debris left on cell surfaces from microbubble based ultrasound molecular imaging. *Ultrasonics* **54**, 2090–2098 (2014).
64. Leow, R. S., Wan, J. M. F. & Yu, A. C. H. Membrane blebbing as a recovery manoeuvre in site-specific sonoporation mediated by targeted microbubbles. *J. R. Soc. Interface* **12**, (2015).
65. van Rooij, T. *et al.* Viability of endothelial cells after ultrasound-mediated sonoporation: Influence of targeting, oscillation, and displacement of microbubbles. *J. Control. Release* **238**, 197–211 (2016).
66. Crake, C. *et al.* Passive acoustic mapping of magnetic microbubbles for cavitation enhancement and localization. *Phys. Med. Biol.* **60**, 785–806 (2015).
67. Lee, J. Y. *et al.* Ultrasound-Enhanced siRNA Delivery Using Magnetic Nanoparticle-Loaded Chitosan-Deoxycholic Acid Nanodroplets. *Adv. Healthc. Mater.* **6**, (2017).
68. Lum, A. F. H. *et al.* Ultrasound radiation force enables targeted deposition of model drug carriers loaded on microbubbles. *J. Control. Release* **111**, 128–134 (2006).
69. Dayton, P., Klibanov, A., Brandenburger, G. & Ferrara, K. Acoustic radiation force in vivo: A mechanism to assist targeting of microbubbles. *Ultrasound Med. Biol.* **25**, 1195–1201 (1999).
70. Kaya, M. *et al.* Acoustic Radiation Force for Vascular Cell Therapy: In Vitro Validation. *Ultrasound Med. Biol.* **38**, 1989–1997 (2012).
71. Park, Y. C. *et al.* Microvessels-on-a-chip to assess targeted ultrasound-assisted drug delivery. *ACS Appl. Mater. Interfaces* **8**, 31541–31549 (2016).
72. Helfield, B., Chen, X., Watkins, S. C. & Villanueva, F. S. Biophysical insight into mechanisms of sonoporation. *Proc. Natl. Acad. Sci.* **113**, 9983–9988 (2016).
73. Qin, P., Han, T., Yu, A. C. H. & Xu, L. Mechanistic understanding the bioeffects of ultrasound-driven microbubbles to enhance macromolecule delivery. *Journal of Controlled Release* **272**, (2018).
74. Song, K.-H., Harvey, B. K. & Borden, M. A. State-of-the-art of microbubble-assisted blood-brain barrier disruption. *Theranostics* **8**, 4393–4408 (2018).
75. McDannold, N., Arvanitis, C. D., Vykhodtseva, N. & Livingstone, M. S. Temporary disruption of the blood-brain barrier by use of ultrasound and microbubbles: Safety and efficacy evaluation

- in rhesus macaques. *Cancer Res.* **72**, 3652–3663 (2012).
76. Rouwkema, J., Koopman, B. F. J. M., Blitterswijk, C. A. V., Dhert, W. J. A. & Malda, J. Supply of nutrients to cells in engineered tissues. *Biotechnol. Genet. Eng. Rev.* **26**, 163–178 (2009).
 77. Forster, J., Harriss-Phillips, W., Douglass, M. & Bezak, E. A review of the development of tumor vasculature and its effects on the tumor microenvironment. *Hypoxia* **Volume 5**, 21–32 (2017).
 78. De Moor, L. *et al.* High-throughput fabrication of vascularized spheroids for bioprinting. *Biofabrication* **10**, (2018).
 79. Hasan, A. *et al.* Microfluidic techniques for development of 3D vascularized tissue. *Biomaterials* **35**, 7308–7325 (2014).
 80. Albanese, A., Lam, A. K., Sykes, E. A., Rocheleau, J. V. & Chan, W. C. W. Tumour-on-a-chip provides an optical window into nanoparticle tissue transport. *Nat. Commun.* **4**, (2013).
 81. Ozcelikkale, A., Moon, H. R., Linnes, M. & Han, B. In vitro microfluidic models of tumor microenvironment to screen transport of drugs and nanoparticles. *Wiley Interdisciplinary Reviews: Nanomedicine and Nanobiotechnology* **9**, (2017).